

CHALCOGENIDE INVERTED OPAL PHOTONIC CRYSTAL AS INFRARED PIGMENTS

A. E. ALIEV*, A. A. ZAKHIDOV and R. H. BAUGHMAN
Nanotech Institute, University of Texas at Dallas
2601 North Floyd Rd., Richardson, TX 75083, USA
*Ali.Aliev@utdallas.edu

E. YABLONOVITCH
Electrical Engineering Department, University of California
Los Angeles, CA 90095, USA

Revised 13 February 2006

Large surface infrared photonic crystals with reflectance higher than 90% have successfully been synthesized by self-assembling large size SiO_2 spheres, of 0.8–4.5 μm diameters, followed by melt infiltration with the chalcogenide glass $\text{Ge}_{33}\text{As}_{12}\text{Se}_{55}$ and the removal of the SiO_2 spheres by chemical etching. The sphere size and the periodicity of the templates were chosen to guarantee the formation of photonic band gaps of the inverted opals in the targeted IR regions of 3–5 μm and 8–12 μm . Fabrication, structural features and spectral behavior of the reflectance peaks of these chalcogenide glass inverse opals are presented.

Keywords: Photonic crystals; synthetic opal; self-assembling.

1. Introduction

Since the introduction of photonic crystals (PC) concept by Yablonovitch¹ and John,^{2,3} these structures have attracted steadily increasing interest and attention from the research community. The behavior of photons in PC is very analogous to electrons in semiconductors: the photonic band structure may show forbidden gaps in which photons cannot exist, therefore many of the devices and concepts based on the band gap phenomena in semiconductors may be extended to PC. PC can be defined as mesoporous materials with a periodic distribution of submicrometric pores. There are three parameters that are critical for the existence of a photonic bandgap (PBG). First, the refractive index contrast, defined as the ratio between the refractive indices of the material and the surrounding substance; secondly, the filling fraction, defined as the percentage volume occupied by the voids; and finally the topology of the PC structure will also be critical in the formation of the PC band structure. The most common method of fabricating them is the micro-machining of a bulk material by lithographic methods, but this approach is so

* Corresponding author.

expensive and time consuming that only the creation of PC of a few monolayers are technically achievable at present.^{4,5} It is also difficult to obtain a complete gap in PC in a particular spectral region.

An alternative route involves using self-assembly methods to achieve opal-like structures.^{6–9} Opals are gemstones formed through the settlement of monodisperse submicrometer silica particles. As a consequence of periodicity, they show opalescence: reflected colors that come from the Bragg diffractions in the periodic distribution of particles. Bragg diffraction constitutes the fingerprint of PBG properties. However, theory predicts that inverse opals would show much better PBG properties than direct opals. Inverse opals can be regarded as the negative replica of opals — micrometer-sized spherical cavities surrounded by a high refractive index material, in which both the cavities and the high refractive material are connected throughout the structure. Recently, we have developed a simple method of fabricating three-dimensional (3D) composite superstructures by using synthetic opals as templates.^{10,11} Here we extend this method to fabricate PCs in the infrared range. Since the conventional synthesis method is not applicable for large size silica spheres, we have developed a method of self-assembly using highly viscous liquids, a silicon substrate bottom with increased cylinder volume and pH of solution, and additional thorough particle purification by repeated resedimentation.

Photonic crystals with periodically modulated refractive index are emerging as useful artificial pigments for camouflage coatings. They can be characterized by lower average emissivity, but they have a controlled spectral dependence. At infrared wavelengths, heat emitting systems are easily recognizable by night vision systems utilizing the infrared atmospheric windows of 3–5 μm and 8–12 μm . A combination of high reflectance in targeted IR range and transparency at other regions for release the heat will make it possible for heat-generating objects equipped with a coating of these PCs to adaptively blend into the infrared environment.

In this paper, we report the progress in the development of self-assembling and templating techniques for the synthesis of infrared photonic crystals for the 3–5 μm and 8–12 μm IR atmospheric windows. The generic concept we developed for creating this IR physical pigment includes the self-assembly of 3D silica opal layers, sintering of the layers, infiltration of the silica opal with IR transparent material and finally dissolving the SiO_2 spheres to leave the inverse opal structure. A chalcogenide glass system $\text{Ge}_{33}\text{As}_{12}\text{Se}_{55}$ exhibiting high IR transparency and other desired optical, chemical and thermal properties was infiltrated into porous silica opal structures having silica sphere diameters of 0.8, 2.28, 3.65, and 4.5 μm . Surface images and the comparison of the spectral characteristic of bare, melt infiltrated and obtained inverse opals are presented.

2. Experimental

2.1. Fabrication process details

Monodispersed silica spheres with diameters of 2.28, 2.4, 2.8, 3.01, 3.9, 4.5, 5.0 and 6.0 μm were purchased from Bangs Laboratories, Inc. (www.bangslabs.com). To achieve

highly crystalline FCC structure, the silica particles were thoroughly purified by repeated sedimentation from a water suspension. Even after five resedimentation cycles, there were still quite a few defected particles: twins and “bitten” spheres.

The sedimentation velocity is an extremely important parameter in achieving an ordered array of colloidal particles. It is known that when gravitational energy is much larger than thermal energy (k_bT), the sedimentation occurs far from equilibrium and noncrystalline sediment is obtained.^{12,13} To reduce the sedimentation velocity of the large size particles, we used ethylene glycol ($\rho = 1.113 \text{ g/cm}^3$, $\eta = 16.1 \text{ mPa}\cdot\text{s}$).

The sedimentation velocity is determined from the balance of gravitational ($F_g = (1/6)\pi\rho_s g d^3$), Archimedes ($F_A = (1/6)\pi\rho_w g d^3$), and frictional forces ($F_f = 3\pi\eta v d$), where ρ_s and ρ_w are the sphere and water mass densities, g is the gravity acceleration, η is the viscosity of liquid, D is the sphere diameter, and V is their velocity.

$$V = \frac{D^2(\rho_s - \rho_w)g}{18\eta}. \quad (1)$$

For example, for $2.8 \mu\text{m}$ silica particles with density of 1.96 g/cm^3 suspended in water, the theoretical sedimentation velocity is 16.6 mm/h , but our first experimental value monitored by the descended height of colloid/clear water interface for nonpurified particles was much lower, 7.2 mm/h . After six repeated sedimentation and dispersion, the velocity increased to 10.6 mm/h and the colloid/clear water interface became much sharper. Figure 1 shows sedimentation velocity versus particle diameter for water

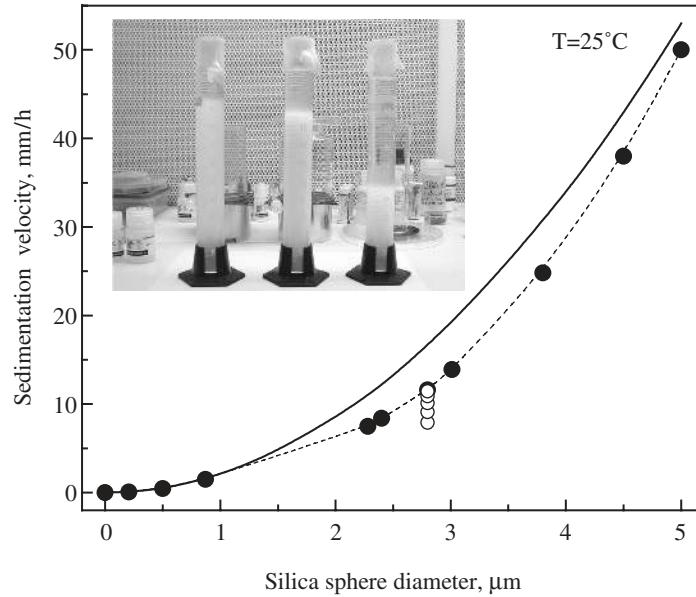


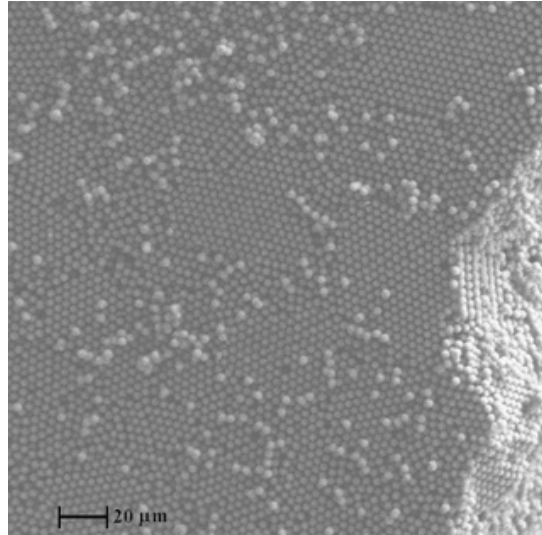
Fig. 1. Sedimentation velocity versus silica particles diameter. The solid line represents the ideal model of noninteracting particles according to Eq. (1), solid circles represent experimentally measured results. The open circles show the change in sedimentation velocity measured after each purification steps, for a given sphere size, $D = 2.8 \mu\text{m}$.

suspensions. Purification brings the monitored values closer to the classical Stokes law shown by solid line. Nevertheless the experimentally obtained sedimentation velocities are lower than predicted by Eq. (1). One of the possible reasons is a particle interaction in the high density suspension while Eq. (1) assumes noninteracting particles.

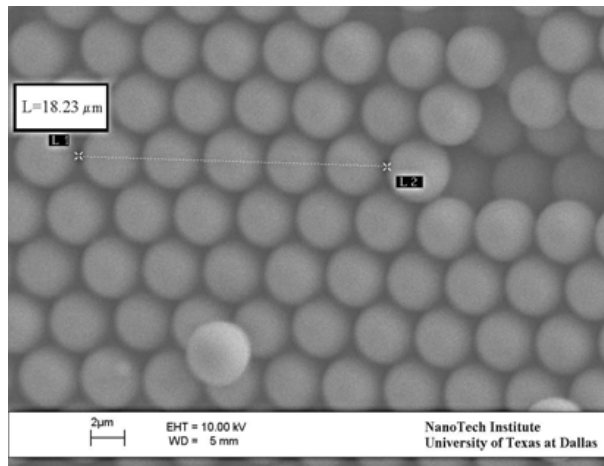
A large deviation of particle sizes within a suspension might also account for the decrease in sedimentation velocity as a result of the friction between larger particles and smaller ones. The same purified $2.8\ \mu\text{m}$ particles in ethylene glycol suspension had a sedimentation velocity of $0.8\ \text{mm/h}$ at $T = 25^\circ\text{C}$, which is close to the desired velocity $0.4\ \text{mm/h}$.¹⁴

The first precipitation trial of $3.9\ \mu\text{m}$ SiO_2 spheres in pure ethylene glycol suspension onto a glass substrate in a glass cylinder ($D = 15\ \text{mm}$, $H = 60\ \text{mm}$) gave an almost amorphous structure. The reason of this failure was determined as due to low repulsive forces between silica spheres and low surface mobility of particles on rough substrate. So we have chosen a silicon substrate (attached to the bottom of sedimentation glass cylinder by epoxy glue) to provide a near-perfectly flat surface for sedimentation and to enable the substrate with precipitate layer to be detached from the glass cylinder for sintering directly on the same silicon substrate. The sizes of silica particles used are easily resolved by optical microscopy. We found that the surface tension at the cylinder wall causes the distortion of crystal structure at the distance of $3\text{--}5\ \text{mm}$ from the edge. To overcome this problem, we increased the cylinder diameter to $80\ \text{mm}$ and decreased the suspension concentration by increasing the suspension depth up to $200\ \text{mm}$ (greater depth gives the particles more time, via Brownian motion, to reach equilibrium and to find optimal position within the ordered layer). To increase the repulsive electrostatic interaction between suspended colloidal spheres, we increased the pH of the solution up to 8.5 by adding NaOH pallets to the ethylene glycol. The resulting close-packed f.c.c. lattice of silica spheres with a typical domain size of $100\ \mu\text{m}$ is shown in Fig. 2.

The as-grown and dried at room temperature opal is a solid but it is chalk-like in a sense of mechanical properties, i.e., not strong enough to provide mechanical integrity. The opal was dried at 120°C in a tightly closed cylinder for $48\ \text{h}$. Slow drying at high humidity protects the opal layer from deformation and cracking. For the high temperature sintering, the silicon substrate with the deposited opal layer was carefully detached from cylinder bottom and was placed into the furnace. The sintering is necessary to make precipitated slab hard enough for further melt infiltration and to create necks between spheres. These necks provide the intersphere interconnections that allow SiO_2 spheres to be chemically removed after infiltration.¹⁰ The annealing temperature and duration are highly dependant on the sphere size. For the SiO_2 spheres of diameter $D = 250\ \text{nm}$, the optimal annealing parameters were: $T = 750^\circ\text{C}$, $t = 4\ \text{h}$.¹⁰ For $2.28\text{--}4.5\ \mu\text{m}$ silica spheres, we used $T = 900^\circ\text{C}$ with a sintering time varied from $10\ \text{h}$ to $48\ \text{h}$, respectively. Thermal annealing of bulk samples with the thickness more than $1\ \text{mm}$ for large silica spheres ($> 1\ \mu\text{m}$) usually causes the sample to crack, so we limited the thickness of our deposited layers to $0.5\ \text{mm}$.



(a)



(b)

Fig. 2. SEM image of a sintered opal template fabricated from silica microspheres of $3.9 \mu\text{m}$. (a) Low-magnification image showing long-range ordering. Several ordered layers can be seen on the fractured edge to the bottom right. (b) High-magnification image showing a decrease in the lattice parameter: after sintering at 900°C for 24h, the average distance between spheres reduced from $3.9 \mu\text{m}$ to $3.65 \mu\text{m}$.

2.2. Infiltration

Among the variety of infrared materials, the chalcogenide glass systems $\text{As}_x\text{S}_{1-x}$, $\text{As}_x\text{Se}_{1-x}$ and $\text{Ge}_x\text{As}_{1-x}\text{Se}_y$ are very attractive for photonic application. The high optical transmission

Table 1. Some physical properties of chalcogenide glass AMTIR-1 and other close related glasses given for comparison.^{15–17}

Name	Formula	Refraction index	Transmission range (μm)	Melting point ($^{\circ}\text{C}$)
AMTIR-1*	$\text{Ge}_{33}\text{As}_{12}\text{Se}_{55}$	2.514 ($4\mu\text{m}$) 2.497 ($10\mu\text{m}$)	0.9–16	370
Arsenic selenide	As_2Se_3	2.41 ($4\mu\text{m}$)	2.0–12	260
Arsenic sulfide	As_2S_3	2.41 ($5\mu\text{m}$)	1.5–8	310
Gallium Arsenide	GaAs	3.3 ($4\mu\text{m}$)	1.0–15	1238
	$\text{Ge}_{25}\text{Ga}_5\text{As}_5\text{S}_{65}$	2.58	0.6–7	850

*<http://www.amorphousmaterials.com/Amtir-1.htm>.

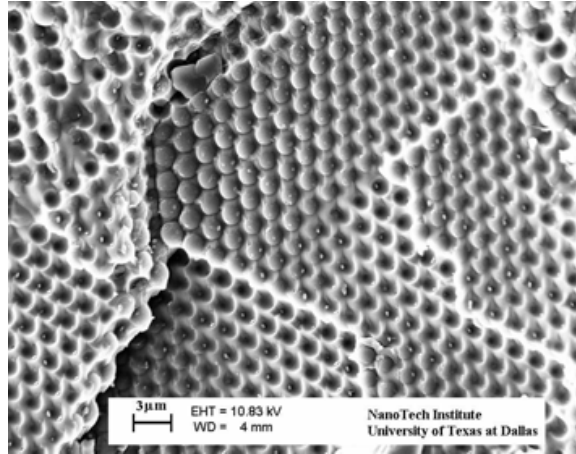
(> 60%) in the spectral range of 2 to $12\mu\text{m}$, high refractive indexes and low melting temperatures make them the perfect materials for IR PCs. Some relevant parameters for these glass systems are given in Table 1.

$\text{Ge}_{33}\text{As}_{12}\text{Se}_{55}$ (brand name AMTIR-1) was obtained from Amorphous Materials, Inc. (<http://www.amorphousmaterials.com>) and infiltrated into the opals by melt infiltration. In a typical preparation process,¹¹ round plates of opal with diameter of 5 mm and a thickness 0.5 mm were surrounded with AMTIR-1 powder that tightly filled the 8 mm diameter aluminum cylinder. Five or six stacked plates were placed with powder layers between them to avoid damage and improve the filling factor of the inner plates. Using a piston-cylinder pressure cell, this cylinder was held at 600°C under pressure of 250 bars for 30 min. During this time, the chalcogenide melt entirely filled the void spaces available through the interconnection. The pressure was lowered during solidification and then was completely released once the piston-cylinder was cooled down to ambient temperature. The infiltrated opal sample was then carefully cut to 1 mm slices using a jeweler's saw and polished. Figure 3(a) shows the SEM image of the cleft edge of $2.28\mu\text{m}$ infiltrated opal. Some part of silica spheres are removed, opening the perfect crystalline structure of chalcogenide glass voids.

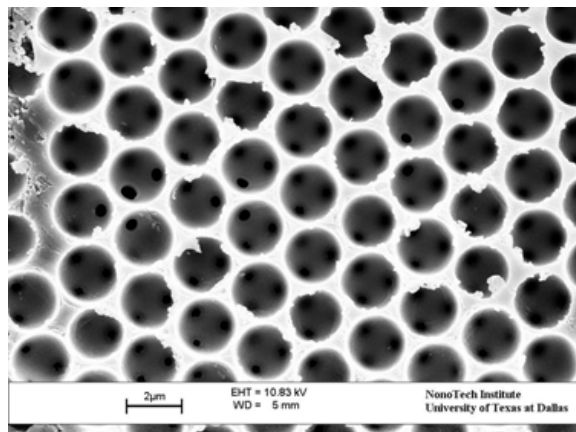
Finally, the inverse opal was obtained by chemically removing the silica. Samples were placed in a 1%HF in water solution for 10 h. The connectivity of the silica template, caused by sintering, allows the acid solution to flow through the structure as the silica is etched away. The resulting chalcogenide glass inverse opal structure for sphere size of $2.28\mu\text{m}$ is shown in Fig. 3(b).

2.3. Characterization methods

Electronic micrographs of our opal templates and inverse opal photonic crystals were obtained using a LEO 1530 scanning electron microscope. Prior to SEM imaging, samples were coated with a thin layer of gold using a BOC Edwards Model 306 evaporator. To increase measurement accuracy, we measured lattice constants of the



(a)



(b)

Fig. 3. (a) SEM image of the cleft edge of chalcogenide glass-silica opal composite with $\sim 100\%$ infiltration. (b) Image of the chalcogenide glass inverse opal. The channels between voids are easily seen. The original particle diameter of the template was $2.28\text{ }\mu\text{m}$. After sintering, the distance between particles reduced to $2.00\text{ }\mu\text{m}$.

engineered PCs at each step and averaged the distance between spheres in chains of 5, 10, or 20 spheres (see Fig. 2(b)). Infrared reflection and transmission spectra were taken using a PerkinElmer AutoIMAGE Microscope combined with PerkinElmer Fourier-transform Infrared (FT-IR) spectrometer Spectrum GX. The range of the reflection and transmission spectra extends from $1\text{ }\mu\text{m}$ to $20\text{ }\mu\text{m}$, using a broadband infrared glowbar source, KBr beamsplitter and liquid-nitrogen-cooled MCT detector. The broad collection angle of the microscope provided by high-performance Cassegrain mirror system enabled to capture a large portion ($\sim 65\%$) of the reflected radiation and send it to the detector.

3. Results

The optical properties of the samples at each step of the fabrication process were studied by reflectance spectroscopy in the infrared region of 1–20 μm . For comparison and to see how the step by step engineering of the photonic crystal changed the spectral characteristics, we first examined perfect opal samples with high quality bulk crystalline structure composed of silica spheres of 800 nm provided by Prof. Lidia Kazantseva from Novosibirsk Institute of Minerals, Russia. The average crystalline domain size for these samples was 2 mm in diameter and 10 mm in height along the opal growth direction. Figure 4 shows the reflectance spectra of bare, melt infiltrated and inverse opal for the reference samples. The SEM images are also shown.

Samples were illuminated with unpolarized light through a microscope Cassegrain mirror system so that the spot size (100 $\mu\text{m} \times 100 \mu\text{m}$) was smaller than the typical domain size, and at the same time larger than silica spheres size (0.8 – 4.5 μm). All reflectance spectra were taken from (111) closest-spaced planes. The illumination was roughly along the [111] direction, corresponding to the crystals *L*-point on the first Brillouin zone surface. Due to the Cassegrain mirror system, some part of the light collection cone centered on the optical axis remains blocked. As a result, measurements are not performed at exact normal incidence but integrate direction comprised between two limiting angles, $\theta_1 = 84^\circ$ and $\theta_2 = 55^\circ$. The Cassegrain objective design and two diffracting planes, (111) and (210) of f.c.c opal are shown in Fig. 5.

The wavelength of the reflection peak can be calculated using the simple equation for Bragg diffraction:

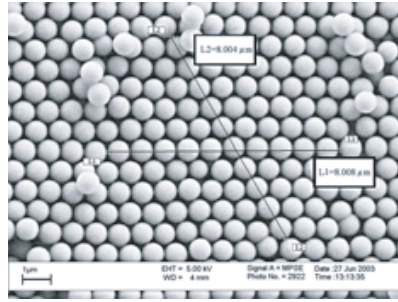
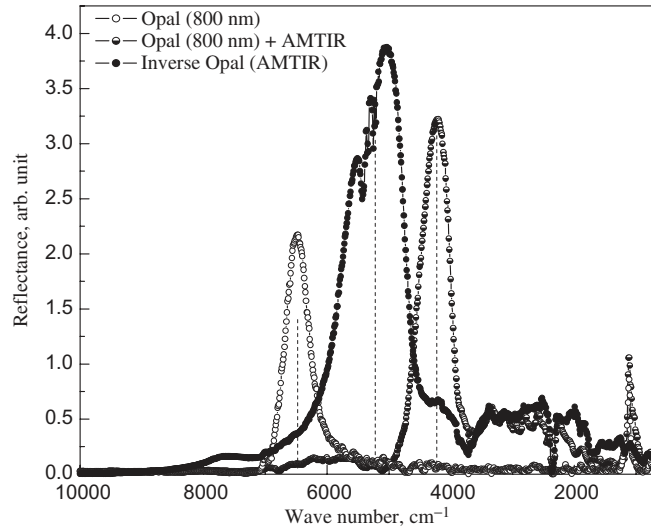
$$\lambda_{\max} = 2d_{111}n_{\text{eff}} \sin \theta, \quad (2)$$

where $d_{111} = (2/3)^{1/2}D$ is the separation between (111) planes, $n_{\text{eff}} = [(n_s)^2 f + (n_p)^2 (1 - f)]^{1/2}$ is an effective refractive index, f is the filling factor of the spheres ($f = 0.74$ for f.c.c structure) and θ is the angle measured from the beam to the planes. It has been shown that the calculated effective refractive index, based on the volume fraction of the respective dielectric components, correlates well with the filling fraction f .

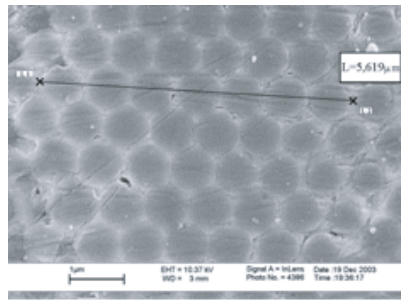
On the other hand, a more precise description of the angular position of the resolved reflection peaks can be done by combination Bragg's law and Snell's law.^{18,19} The modified form of Bragg's law, which takes into account the reduced angle with respect to the normal at which light travels in the opal (i.e., taking into account Snell's law), can be written as:

$$\lambda_{\max} = 2d_{111} \sqrt{n_{\text{eff}}^2 - \sin^2 \varphi}, \quad (3)$$

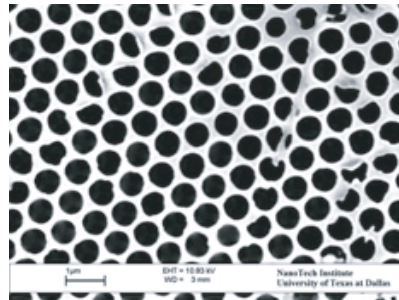
where φ is the angle measured from the normal to the beam. The peak position obtained from our measurements compared fairly well with the results of calculations using Eq. (3). As an input parameters for the calculations, we used $n_{\text{air}} = 1$, $n_s = 1.36$, $n_{\text{glass}} = 2.5$ and corresponding sphere diameters D . The average incident angle φ used for calculations was 30° ($\theta = 70^\circ$). As a result of our calculations by both equations and comparison with experimentally obtained peak position, we found that Eq. (2) produces a systematic



(a)



(b)



(c)

Fig. 4. Reflectance spectra and SEM images of the reference opal with the perfect f.c.c structure. Open circles correspond to a sintered bare opal made of 800 nm average diameter silica spheres (a). The same opal infiltrated with AMTIR-1 shown by semisolid circles, (b) Solid circles correspond to a chalcogenide glass inverted opal structure, (c) The features at 5400 cm^{-1} , 3710 cm^{-1} , and 2300 cm^{-1} are due to H_2O and CO_2 , respectively. Characteristic SiO_2 reflectance peak (high absorption) around 1000 cm^{-1} for bare and infiltrated opal and very small trace for inverted opal glass structure confirm the entire extraction of silica spheres.

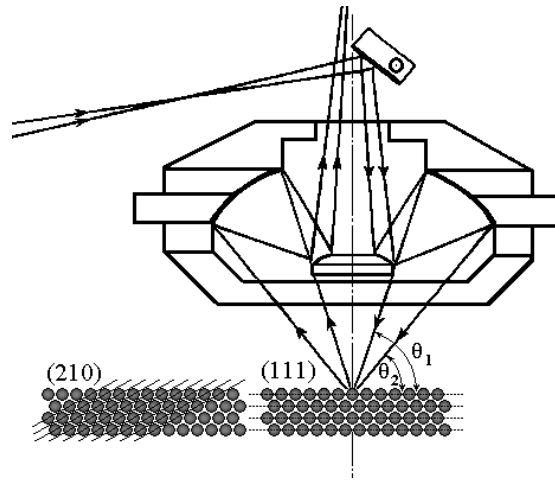


Fig. 5. Diagram of Cassegrain mirror system used in FT-IR system both to direct radiation onto the sample and to collect the reflected signal. The angles θ_1 and θ_2 indicate the size of the annular cone of angles probed by FT-IR. (111) planes give the large reflectance peak and (210) low density tightly stacked planes give the satellite reflectance peaks.

Table 2. Reflectance peak positions calculated and measured for all studied structures using Eq. (3). The refraction indexes of silica spheres and chalcogenide glass have been taken as $n_s = 1.36$, and $n_p = 2.5$, respectively. The average light incident angle has been taken as $\varphi = 30^\circ$.

Sphere size (nm)	Bare opal $n_{\text{eff}} = 1.276$		Infiltrated opal $n_{\text{eff}} = 1.73$		Inverse opal $n_{\text{eff}} = 1.54$	
	Calc. $\text{cm}^{-1}/\mu\text{m}$	Exp. $\text{cm}^{-1}/\mu\text{m}$	Calc. $\text{cm}^{-1}/\mu\text{m}$	Exp. $\text{cm}^{-1}/\mu\text{m}$	Calc. $\text{cm}^{-1}/\mu\text{m}$	Exp. $\text{cm}^{-1}/\mu\text{m}$
Before sintering / after sintering						
824/800	6400/1.566	6470/1.550	4710/2.123	4400/2.27	5290/1.890	5250/1.900
2280/2000	2553/3.915	2560/3.910	1883/5.310	1881/5.310	2120/4.723	2120/4.720
3900/3650	1400/7.141	1450/6.90				
4500/4430	1160/8.615	1165/8.58	851/11.75	850/11.8	956/10.46	960/10.40

overestimation of wavelength of around $\sim 2\%$, consistent with the conclusion in Ref. 20. The results of the calculations of reflectance peak position using Eq. (3) for all of the studied structures are tabulated in Table 2, where they are compared with experimental values. The sphere size before and after sintering shown in the first column was precisely measured by SEM.

All studied structures show the similar spectral behavior. The peak positions of the studied opal structures presented in Table 2 are in an excellent agreement with the calculations by Eq. (3) except the position for infiltrated reference opal. Apparently this deviation is due to a higher porosity of the reference opal, prepared using a different technology. Some part of the infiltrated glass might fill not only octahedral and tetrahedral pores but also the nanopores inside the body of the silica spheres, increasing the overall refractive index.

The measured intensities of reflectance peaks for the bare opal normalized to the specular reflectance intensity of gold film are in the range of 40–50%. Taking into

account the diffusive character of Bragg reflectance from close-packed silica layers and the value of the bulk angle of the Cassegrain collection mirror, we can estimate the actual peak intensity to be 70–80%. Infiltration increases the effective refractive index to $n_{\text{eff}} = 1.73$ and shifts the peak position to lower wave numbers. At the same time, the increase of the contrast ratio from $n_{\text{silica}}/n_{\text{air}} = 1.36$ to $n_{\text{glass}}/n_{\text{silica}} = 1.84$ increases the width of effective PBG and the peak intensity. The extraction of the silica spheres from the infiltrated opals gives a further increase in contrast ratio to $n_{\text{glass}}/n_{\text{air}} = 2.5$ and thus increase the peak intensity up to 60–70%. However, the peak position shifts back to higher wave numbers because of a decrease of the effective refractive index of inverted opal to $n_{\text{eff}} = 1.54$.

Hence, it is worth-while noting that even at low contrast ratio the reflectance of opal structure in the specific frequency range is quite high and close to that of the gold mirror. In Fig. 6. the reflectance peak for infiltrated opal is compared with reflectivity of highly polished chalcogenide glass AMTIR-1. Although the PBG is well recognizable in transmission spectra in Fig. 6, the transmittance is very low compared to the bare glass (60%) for both infiltrated and inverted opals.

In our Cassegrain mirror system, the angle of incident light is distributed in the range $\theta_1 - \theta_2 = 29^\circ$ (see Fig. 5). The corresponding band due to the instrumental broadening of

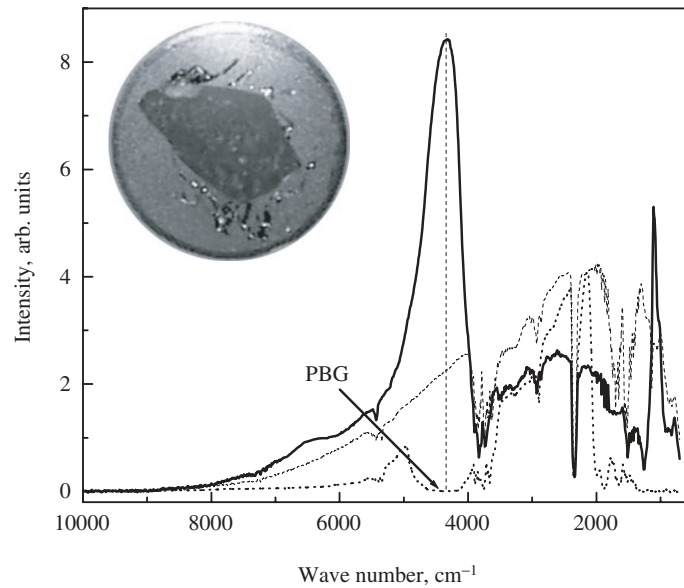


Fig. 6. Comparison of reflectance spectra of infiltrated 800 nm opal structure (solid line) with reflectance of bulk high polished chalcogenide glass AMTIR-1 (dashed line). The dotted line corresponds to the transmission spectra taken from the same region as the reflectance spectra of 0.5 mm thick sample. Inset shows a picture of a polished slice of an 800 nm opal infiltrated with AMTIR-1. The dark (brown) color sample in center is surrounded by the gray color chalcogenide glass.

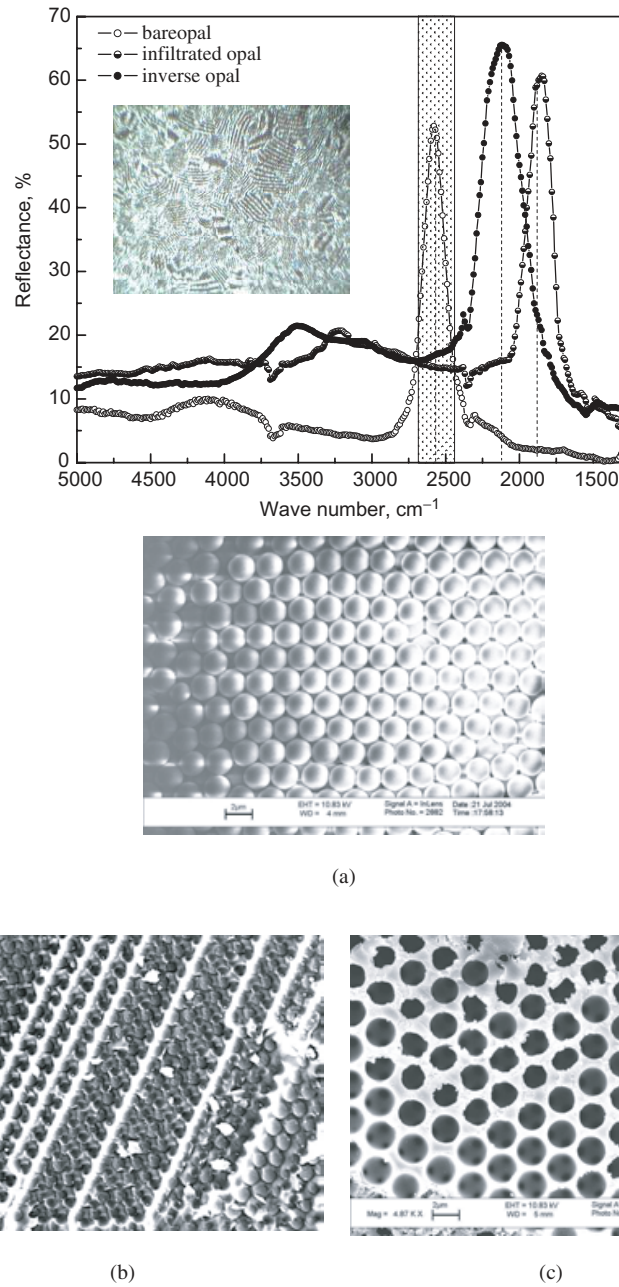
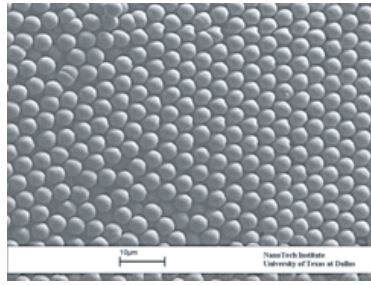
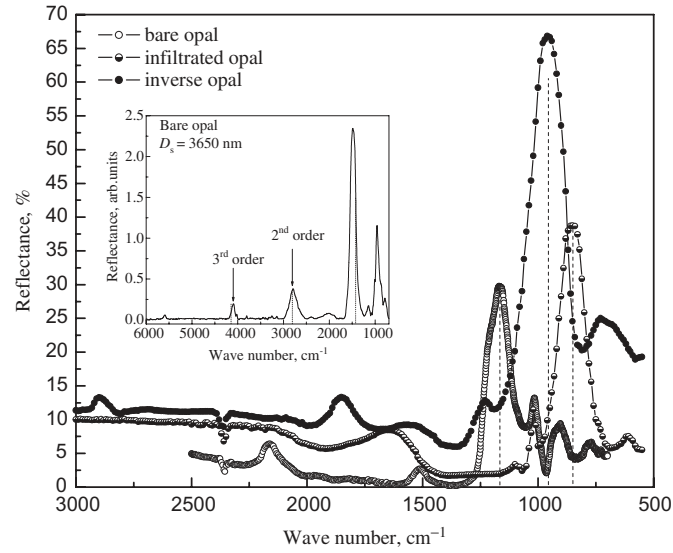
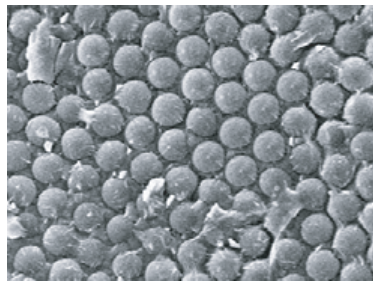


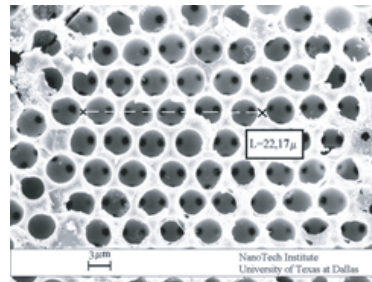
Fig. 7. Reflectance spectra of the bare opal (open circles) with sphere size 2280 nm, opal infiltrated with AMTIR-1 glass (semisolid circles), and chalcogenide glass inverted structure (solid circles). The SEM images of the corresponding structures as shown as (a), (b), and (c), respectively. The wide annular angle of incident and collecting light of the Cassegrain mirror system distributed in radial direction to 29° gives the instrumental broadening of the reflectivity peak shown by shaded strip. The inset shows the FT-IR microscope image of domain structure of inverse opal.



(a)



(b)



(c)

Fig. 8. Reflectance spectra of the bare opal (open circles) with sphere size 4500 nm, opal infiltrated with AMTIR-1 glass (semisolid circles), and chalcogenide glass inverted structure (solid circles). The corresponding SEM images are shown as (a), (b), and (c), respectively. The inset shows the reflectance spectra of the bare opal with sphere size 3650 nm (3900 nm before sintering). The calculated position of the reflectance peak of first order ($1400 \text{ cm}^{-1}/7.141 \mu\text{m}$), second order ($2800 \text{ cm}^{-1}/3.57 \mu\text{m}$), and third order ($4200 \text{ cm}^{-1}/2.38 \mu\text{m}$) shown by dot lines.

the reflectivity peak calculated using Eq. (3) is exactly covering the measured peak (Fig. 7, shaded strip). Obviously, the real reflectance peak width is much narrower. This comparison provides additional evidence of a high quality of internal structural order in the created opals. Although the contrast ratio of 2.5 is not enough for opening of full photonic band gap, the increase of contrast ratio in our technological process from 1.36 to 1.84 and finally to 2.5 widens the reflectance peak to $\Delta\lambda_{2,28} = 5.34\text{--}4.24\ \mu\text{m}$ and $\Delta\lambda_{4,5} = 12\text{--}8.83\ \mu\text{m}$, respectively. The frequency band gap $\Delta\nu$ for nonabsorbed materials is determined by the contrast ratio between the refractive index of host n_h and guest n_g materials²¹ as $\Delta\nu/\nu_o \approx |n_h - n_g|/n_{\text{eff}}$. The calculated value of $\Delta\nu$ for all the studied structures is much higher than an experimentally obtained value. It is worth-while noting that the width of reflectance peak for carbon inverse opal is much wider, indicating the high absorption and reduced light penetration depth. The elevated background at wave numbers higher than the reflectance peak position (for 800 nm, opals background was subtracted) perhaps originated from intense scattering from the large spheres as well as impurities.

All our structures show an additional weak reflectance peak at higher wave numbers. The shift of those peaks at glass infiltration and extraction SiO_2 spheres is the same as for reflectance peaks from the (111) plane. Our investigation shows that these peaks belong to (210) plane as shown in Fig. 5. The width of the corresponding PGB is narrower than in other directions.²² This facet has a very low density, formed by stretched hexagons. These planes are tightly stacked (spacing $0.63D$), have a closest angle to (111) planes.

The mapping of reflectivity intensity over the whole sample surface, shown in the inset of Fig. 7, reveals the very interesting advantage of domain structure: each domain has a reflectance maximum in a slightly different direction. Thus, the average visual reflectance that will appear in night vision devices is independent of the observation angle. In addition to the above mentioned first order diffraction peaks, some perfect structures also show several higher order diffractions. Three orders of diffraction peaks are recognizable in the inverse opal with sphere size of 4500 nm, as shown in Fig. 8 as well as for the bare opal with sphere size of 3650 nm (Fig. 7, inset).

4. Conclusions

We have successfully fabricated chalcogenide glass inverse opals with photonic band gaps spectrally tuned to the desired regions of the infrared atmospheric transparency windows of 3–5 μm and 8–12 μm . Large surface area infrared photonic crystals with reflectance higher than 90% were synthesized by self-assembling large SiO_2 spheres of 0.8–4.5 μm diameters, followed by melt infiltration with chalcogenide glass $\text{Ge}_{33}\text{As}_{12}\text{Se}_{55}$ and then the extraction of the SiO_2 spheres by chemical etching in 1%HF.

We have demonstrated that the purification of the available market silica monodispersed particles by repeated resedimentation accompanied by steady reduction of the sedimentation velocity and using high viscose liquid resulted in highly ordered 3D arrays of silica microspheres. Reflection spectra measured at each step of the fabrication process are in excellent agreement with the modified form of Bragg's law, which takes

into account the reduced angle with respect to the normal at which light travels in the opal (i.e., taking into account Snell's law).

Acknowledgments

The authors would like to thank Prof. Lidia Kazantseva for useful discussions on the opal growth conditions and for providing the reference samples of 800 nm periodicity opals, and Dr. Sergey Lee for the help with SEM imaging and other valuable contributions. This work was supported by the US Army Research Office through the MURI grant DAAD19-99-1-0316.

References

1. E. Yablonovitch, *Phys. Rev. Lett.* **58**, 2059 (1987).
2. S. John, *Phys. Rev. Lett.* **58**, 2486 (1987).
3. S. John and T. Quang, *Phys. Rev. Lett.* **78**, 1888 (1997).
4. S. Y. Lin, J. G. Fleming, D. L. Hetherington, B. K. Smith, R. Biswas, K. M. Ho, M. M. Sigalas, W. Zubrzycki, S. R. Kurtz and J. Bur, *Nature* **394**, 251 (1998).
5. N. Yamamoto, S. Noda and A. Chutinan, *Jpn. J. Appl. Phys.* **37**, L1052 (1998).
6. W. L. Vos, R. Sprik, A. van Blaaderen, A. Imhof, A. Langendijk and G. H. Wegdam, *Phys. Rev. B* **53**, 16231 (1996).
7. V. N. Bogomolov, D. A. Kurdyukov, A. V. Prokofiev and S. M. Samoilovich, *JEPT* **63**, 520 (1996).
8. C. Lopez, L. Vazquez, F. Meseguer, R. Mayoral, M. Ocana and H. Miguez, *Superlattices Microstruc.* **22**, 399 (1997).
9. A. van Blaaderen, R. Ruel and P. Wiltzius, *Nature* **385**, 321 (1997).
10. A. A. Zakhidov, R. H. Baughman, Z. Iqbal, C. Cui, I. I. Khayrullin, S. O. Dantas, J. Marti and V. G. Ralchenko, *Science* **282**, 897 (1998).
11. A. A. Zakhidov, R. H. Baughman, I. I. Khayrullin, I. A. Udod, M. Kozlov, N. Eradat, V. Z. Vardeny, M. Sigalas and R. Biswas, *Synthetic Mater.* **116**, 419 (2001).
12. H. Miguez, F. Meseguer, C. Lopez, M. Holgado, G. Andreassen, A. Mifsud and V. Fornes, *Langmuir* **16**, 4405 (2000).
13. A. Blanco, E. Chomski, S. Grabtchak, M. Ibisate, S. John, S. W. Leonard, C. Lopez, F. Meseguer, H. Miguez, J. P. Mondla, G. A. Ozin, O. Toader and H. M. van Driel, *Nature* **405**, 437 (2000).
14. M. Holgado, F. Garcia-Santamaria, A. Blanco, M. Ibisate, A. Cintas, H. Miguez, C. J. Serna, C. Molpeceres, J. Requena, A. Mifsud, F. Meseguer and C. Lopez, *Langmuir* **15**, 4701 (1999).
15. S. Shtutina, M. Klebanov, V. Lyubin, S. Rosenwaks and V. Volterra, *Thin Solid Films* **261**, 263 (1995).
16. G. C. Chern and I. Lauks, *J. Appl. Phys.* **53**, 6979 (1982).
17. D. Lezal, J. Pedlikova and J. Zavadil, *J. Optoelectron. Adv. Mater.* **6**, 133 (2004).
18. V. Yannopapas, N. Stefanou and A. Modinos, *J. Phys.: Cond. Matt.* **9**, 10260 (1997).
19. M. Allard, E. Sargent, E. Kumacheva and O. Kalinina, *Optical and Quantum Electronics* **34**, 27 (2002).
20. A. Reynolds, F. Lopez-Tejeira, D. Cassagne, F. J. Garcia-Vidal, C. Jouanin and J. Sanchez-Dehesa, *Phys. Rev. B* **60**, 11422 (1999).

21. J. D. Joannopoulos, R. Meade and J. Winn, *Photonic Crystals: Molding the Flow of Light* (Princeton University Press, Princeton, NJ, 1995).
22. E. Palacios-Lidon, A. Blanco, M. Ibisate, F. Meseguer, C. Lopez and J. Sanches-Dehesa, *Appl. Phys. Lett.* **81**, 4925 (2002).